

REPORT DOCUMENTATION PAGE			Form Approved OMB NO. 0704-0188		
<p>The public reporting burden for this collection of information is estimated to average 1 hour per response, including the time for reviewing instructions, searching existing data sources, gathering and maintaining the data needed, and completing and reviewing the collection of information. Send comments regarding this burden estimate or any other aspect of this collection of information, including suggestions for reducing this burden, to Washington Headquarters Services, Directorate for Information Operations and Reports, 1215 Jefferson Davis Highway, Suite 1204, Arlington VA, 22202-4302. Respondents should be aware that notwithstanding any other provision of law, no person shall be subject to any penalty for failing to comply with a collection of information if it does not display a currently valid OMB control number.</p> <p>PLEASE DO NOT RETURN YOUR FORM TO THE ABOVE ADDRESS.</p>					
1. REPORT DATE (DD-MM-YYYY) 08-07-2010		2. REPORT TYPE Final Report		3. DATES COVERED (From - To) 1-Jul-2005 - 30-Jun-2010	
4. TITLE AND SUBTITLE Formation of Defect Microstructures and Electrical Transport in VOx			5a. CONTRACT NUMBER		
			5b. GRANT NUMBER W911NF-05-C-0070		
			5c. PROGRAM ELEMENT NUMBER 611102		
6. AUTHORS Zhi Gang Yu, Senior Research Physicist			5d. PROJECT NUMBER		
			5e. TASK NUMBER		
			5f. WORK UNIT NUMBER		
7. PERFORMING ORGANIZATION NAMES AND ADDRESSES SRI International 333 Ravenswood Ave., Menlo Park, CA 94025 -			8. PERFORMING ORGANIZATION REPORT NUMBER		
9. SPONSORING/MONITORING AGENCY NAME(S) AND ADDRESS(ES) U.S. Army Research Office P.O. Box 12211 Research Triangle Park, NC 27709-2211			10. SPONSOR/MONITOR'S ACRONYM(S) ARO		
			11. SPONSOR/MONITOR'S REPORT NUMBER(S) 48442-EL.1		
12. DISTRIBUTION AVAILABILITY STATEMENT Approved for Public Release; Distribution Unlimited					
13. SUPPLEMENTARY NOTES The views, opinions and/or findings contained in this report are those of the author(s) and should not be construed as an official Department of the Army position, policy or decision, unless so designated by other documentation.					
14. ABSTRACT This report summarizes SRI's accomplishments from 07/01/05 to 06/30/10 on the, "Formation of Defect Microstructures and Electrical Transport in VOx" project. We have successfully carried out all tasks identified in our initial proposal and supplements and gained significant knowledge and understanding of electrical transport, optical properties, and electronic structures in vanadium oxide (VOx), the most favored material for uncooled microbolometers, and in related highly disordered systems. We have developed algorithms and quantitative					
15. SUBJECT TERMS infrared detection, electrical transport, disordered systems, noise, bolometers					
16. SECURITY CLASSIFICATION OF:			17. LIMITATION OF ABSTRACT UU	15. NUMBER OF PAGES	19a. NAME OF RESPONSIBLE PERSON Zhi-Gang Yu
a. REPORT UU	b. ABSTRACT UU	c. THIS PAGE UU			19b. TELEPHONE NUMBER 650-859-6456

Report Title

Formation of Defect Microstructures and Electrical Transport in VOx

ABSTRACT

This report summarizes SRI's accomplishments from 07/01/05 to 06/30/10 on the, "Formation of Defect Microstructures and Electrical Transport in VOx" project. We have successfully carried out all tasks identified in our initial proposal and supplements and gained significant knowledge and understanding of electrical transport, optical properties, and electronic structures in vanadium oxide (VOx), the most favored material for uncooled microbolometers, and in related highly disordered systems. We have developed algorithms and quantitative modeling tools that compute a variety of transport properties and their dependence on defect microstructures in VOx. These tools are valuable for identifying VOx with appropriate compositions and defect structures for improved bolometer performance. Some of our results have been published in peer-reviewed journals and presented at professional conferences. In addition, we have established a close collaboration with experimentalists in both academia [the Multidisciplinary University Research Initiative (MURI) team led by Prof. Mark Horn at Pennsylvania State University] and industry (Dr. A. J. Syllaios from L3 Communications), who have been working on VOx and related systems. We have provided our understanding and physical insights to the experimentalists and helped analyze their experimental measurements. The collaboration with experimentalists has also broadened our research scope and helped us focus on the most relevant issues concerning VOx

List of papers submitted or published that acknowledge ARO support during this reporting period. List the papers, including journal references, in the following categories:

(a) Papers published in peer-reviewed journals (N/A for none)

None

Number of Papers published in peer-reviewed journals: 0.00

(b) Papers published in non-peer-reviewed journals or in conference proceedings (N/A for none)

None

Number of Papers published in non peer-reviewed journals: 0.00

(c) Presentations

None

Number of Presentations: 0.00

Non Peer-Reviewed Conference Proceeding publications (other than abstracts):

None

Number of Non Peer-Reviewed Conference Proceeding publications (other than abstracts): 0

Peer-Reviewed Conference Proceeding publications (other than abstracts):

R. DeWames, Z. G. Yu, and D. Lohrman, "Electrical conduction and long relaxation times in non-crystalline VOx and ?-Si:H microbolometer infrared detectors," Proc. MSS 2010.

Z. G. Yu and M. A. Berding, "Numerical simulation of 1/f noise in VOx for microbolometers," Proc. MSS 2010.

Number of Peer-Reviewed Conference Proceeding publications (other than abstracts): 2

(d) Manuscripts

R. E. DeWames, A. J. Syllaios, Z. G. Yu, and M. A. Berding, "Distinct electrical transport mechanisms in noncrystalline VOx and a-Si:H," to be submitted to Appl. Phys. Lett.

Number of Manuscripts: 1.00

Patents Submitted

None

Patents Awarded

None

Graduate Students

<u>NAME</u>	<u>PERCENT SUPPORTED</u>
FTE Equivalent:	
Total Number:	

Names of Post Doctorates

<u>NAME</u>	<u>PERCENT SUPPORTED</u>
FTE Equivalent:	
Total Number:	

Names of Faculty Supported

<u>NAME</u>	<u>PERCENT SUPPORTED</u>
FTE Equivalent:	
Total Number:	

Names of Under Graduate students supported

<u>NAME</u>	<u>PERCENT SUPPORTED</u>
FTE Equivalent:	
Total Number:	

Student Metrics

This section only applies to graduating undergraduates supported by this agreement in this reporting period

The number of undergraduates funded by this agreement who graduated during this period:	0.00
The number of undergraduates funded by this agreement who graduated during this period with a degree in science, mathematics, engineering, or technology fields:.....	0.00
The number of undergraduates funded by your agreement who graduated during this period and will continue to pursue a graduate or Ph.D. degree in science, mathematics, engineering, or technology fields:.....	0.00
Number of graduating undergraduates who achieved a 3.5 GPA to 4.0 (4.0 max scale):	0.00
Number of graduating undergraduates funded by a DoD funded Center of Excellence grant for Education, Research and Engineering:.....	0.00
The number of undergraduates funded by your agreement who graduated during this period and intend to work for the Department of Defense	0.00
The number of undergraduates funded by your agreement who graduated during this period and will receive scholarships or fellowships for further studies in science, mathematics, engineering or technology fields:	0.00

Names of Personnel receiving masters degrees

<u>NAME</u>
Total Number:

Names of personnel receiving PHDs

<u>NAME</u>
Total Number:

Names of other research staff

<u>NAME</u>	<u>PERCENT SUPPORTED</u>
FTE Equivalent:	
Total Number:	

Sub Contractors (DD882)

Inventions (DD882)

Final Report • 30 June 2010

FORMATION OF DEFECT MICROSTRUCTURES AND ELECTRICAL TRANSPORT IN VO_x

SRI Project PO16772

Prepared by:

Zhi Gang Yu, Senior Research Physicist
Applied Optics Laboratory

Prepared for:

U.S. Army Research Office
P.O. Box 12211
Research Triangle Park, NC 27709-2211
Attention: Dr. William Clark

ARO Contract W911NF05C0070

Approved by:

Robert Brown, Director
Applied Optics Laboratory

EXECUTIVE SUMMARY

This report summarizes SRI's accomplishments from 07/01/05 to 06/30/10 on the, "Formation of Defect Microstructures and Electrical Transport in VO_x" project. We have successfully carried out all tasks identified in our initial proposal and supplements and gained significant knowledge and understanding of electrical transport, optical properties, and electronic structures in vanadium oxide (VO_x), the most favored material for uncooled microbolometers, and in related highly disordered systems. We have developed algorithms and quantitative modeling tools that compute a variety of transport properties and their dependence on defect microstructures in VO_x. These tools are valuable for identifying VO_x with appropriate compositions and defect structures for improved bolometer performance. Some of our results have been published in peer-reviewed journals and presented at professional conferences. In addition, we have established a close collaboration with experimentalists in both academia [the Multidisciplinary University Research Initiative (MURI) team led by Prof. Mark Horn at Pennsylvania State University] and industry (Dr. A. J. Syllaios from L3 Communications), who have been working on VO_x and related systems. We have provided our understanding and physical insights to the experimentalists and helped analyze their experimental measurements. The collaboration with experimentalists has also broadened our research scope and helped us focus on the most relevant issues concerning VO_x.

TECHNICAL ACHIEVEMENTS

Uncooled infrared focal plane arrays (IR-FPAs) offer significant advantages over cooled IR-FPAs, including reduced cost, weight, and power. Microbolometer arrays based on VO_x have shown outstanding performance and have displaced cooled IR sensing products in many military and civil applications. The complex nature of VO_x as well as the subtle techniques required to fabricate it, necessitates basic research to create new knowledge and understanding to facilitate rapid improvement in this critical technology. To this end, ARO awarded SRI a contract (Project 48442 EL, Formation of Defect Microstructures and Electrical Transport in VO_x) to perform theoretical studies on structural and transport properties of VO_x . The overall goal of the study was to arrive at a comprehensive understanding of the electronic and lattice structures in VO_x , in particular those associated with defect microstructures, and their effects on temperature- and temporal-dependent electrical transport in VO_x . We have successfully performed all the project tasks and developed physical pictures and modeling tools to describe defect structures, electrical transport, and optical properties in highly disordered VO_x systems. Our achievements in are described in detail below.

1. ELECTRONIC STRUCTURE OF VO_x

Given similarities between VO_x and amorphous Si, it is tempting to apply understanding of α -Si directly to VO_x . However, that approach has encountered many irresolvable difficulties.

1.1 NATURE OF CARRIERS IN VO_x

We noticed that among several significant differences between VO_x and α -Si, the first and foremost is that carriers in the two systems have different origins. In α -Si the conduction and valence bands are made of extended s - or p -orbitals, and a well-defined band gap exists between the conduction and valence bands. Carriers responsible for electrical transport in α -Si occupy the impurity band within the band gap, and electrical conduction takes place either through hopping in the impurity band at low temperatures or activating carriers from the impurity band to the conduction band with extended wave functions at high temperatures. In contrast, carriers in VO_x stay in the d -orbitals, which are much more localized than s - and p -orbitals, and the well-defined conduction and valence bands with extended wave functions are either absent or irrelevant to the electrical transport.

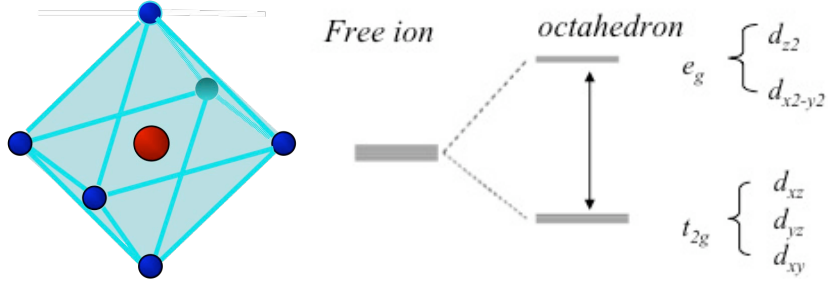


Figure 1 VO_6 octahedron and its energy levels. The red sphere represents the V atom and blue spheres represent oxygen atoms.

To understand the nature of carriers in VO_x , we first examined the electronic structure in stoichiometric vanadium oxides. In VO , V_2O_3 , and VO_2 , each V atom is surrounded by six oxygen atoms, forming an octahedron, in which, the 5-fold degenerate $3d$ orbital splits into a 3-fold degenerate t_{2g} orbital and a 2-fold degenerate e_g orbital (see Fig. 1). The V octahedra in general are distorted, and the triply degenerate t_{2g} further split, to one a_{1g} and one doubly degenerate e_g^π in V_2O_3 and one doubly degenerate π^* and one $c_{||}$. The typical value of this crystal-field splitting between t_{2g} and e_g is large, greater than 3 eV, and the typical splitting between the sub t_{2g} levels is much smaller than 1 eV.

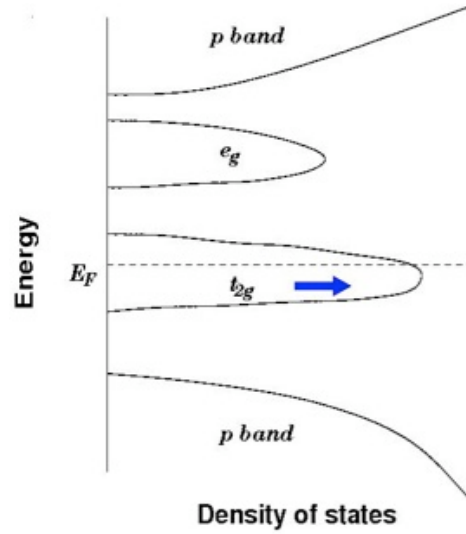


Figure 2 Schematic band structure of VO_x . The dashed line indicates the Fermi energy.

For $x = 1.8$ of VO_x —the commonly used material for an uncooled bolometer—the average valence of V is 3.6, meaning that V ions in the system have mixed valence of $3+$ ($3d^2$) and $4+$ ($3d^1$), and t_{2g} is partially filled. In disordered VO_x , both t_{2g} and e_g states should be localized (Anderson localization) because all come from the same local d orbitals of the V atom. Thus, the process involving thermally excited electrons moving in the e_g band is not effective, which makes VO_x distinct from other amorphous semiconductors like $\alpha\text{-Si}$. Because of the large splitting between t_{2g} and e_g and a much larger splitting between the V d -band and the O p -band, optical transitions with photon energy smaller than 1 eV must take place within the local t_{2g} band, such as from e_g^π to a_{1g} as in V_2O_3 , or from e_g^π to π^* , as in VO_2 (see Fig. 2). Thus the optical gap in VO_x usually does not indicate transitions from a localized state to an extended state in the conduction band as in $\alpha\text{-Si}$. Although optical transitions between 3d orbitals in an isolated atom are dipole-forbidden, the admixture of V 3d orbitals and O 2p orbitals in VO_x makes the transitions possible.

1.2 ELECTRONIC STRUCTURE OF VOX: CLUSTER APPROACH

Although the literature about optical absorption and electric transport in $\alpha\text{-Si}$ is extensive and the underlying electronic structure is fairly well understood, little is known about the semiconductor properties of VO_x for the range of x values used for microbolometer applications. VO_x exhibits unusual optical and transport properties, and a quantitative understanding of those properties is required to fully exploit the strengths of VO_x in IR detection. To date, even a qualitative picture that consistently accounts for both optical and transport properties is lacking.

Studies of VO_x mostly concern $0.8 < x < 1.3$, which can be regarded as perturbations from VO. As Mott first pointed out, these VO_x are disordered systems, and electric conduction is via electron hopping between localized states. Transport measurements indicate that at $x = 0.8$, the material is almost metallic, with the hopping activation energy near zero. As x increases, the activation energy, and accordingly the energy disorder, increases. A large hopping activation energy gives rise to a large temperature coefficient of resistance, which is desired for microbolometers. The typical value of x for VO_x films used in microbolometers is 1.8, which is much closer to VO_2 or V_2O_3 than to VO. Hence, VO_2 serves as a better reference and starting point for considering the properties of VO_x .

Literature addressing VO_x with x close to 1.8 is scarce. We searched the literature and compiled representative data of optical and transport properties of various VO_x , developed a cluster model for VO_x , and verified its validity by comparing theoretical results with measurements.

a. Common Building Block in VO_x: VO₆

In VO_x valence electrons stay in the *d*-orbitals, which are much more localized than the *s*- and *p*-orbitals, and the well-defined conduction and valence bands with extended wave functions are either absent or irrelevant to the electrical transport. This localization is further enhanced by the disorder in an amorphous VO_x film due to Anderson localization, providing a solid justification for a cluster approach. The highly localized *d*-orbitals suggest that an atomic picture is a natural starting point for studying VO_x.

We note that in crystalline VO, V₂O₃, and VO₂, as well as in the Magneli phases of in V_nO_{2n-1}, each V atom is surrounded by six O atoms, forming an octahedron. In the Magneli phases and nonstoichiometric VO_x in general, oxygen vacancies (point defects) are eliminated through the formation of extended planar faults or shear planes, which restores the octahedral coordination of the six O atoms surrounding every V atom. However, different arrangements of some adjacent octahedra from those in the unperturbed lattice result; for example, face-sharing instead of edge-sharing at a shear plane. Thus, the fundamental building block in both stoichiometric and nonstoichiometric vanadium oxides is the VO₆ octahedron.

b. Stoichiometric VO_x: Charged single VO₆ clusters

A V atom has an electronic structure of $3d^3 4s^2$, and the *d*-orbital occupations in VO₂, V₂O₃, and VO are 1, 2, and 3, respectively. In a VO₆ octahedron, the 5-fold degenerate $3d$ orbital splits into a 3-fold degenerate t_{2g} orbital and a 2-fold degenerate e_g orbital, with the gap much greater than 1 eV. Thus, in all these vanadium oxides, t_{2g} is partially occupied. Moreover, electric transport and optical transitions with a photon energy smaller than 1 eV must involve only t_{2g} states. Given that the t_{2g} orbital is a combination of d_{xy} , d_{yz} , and d_{zx} , which form only weak π bonding with the surrounding O *p*-orbitals, the electrons in t_{2g} levels are rather localized compared with e_g states. By studying such clusters, we gained insights into electronic structures of amorphous VO_x, which would be difficult, if not impossible, by employing conventional solid-state band-structure approaches. What distinguishes one vanadium oxide from another in a VO₆ cluster is the effective charge of the system. Because the formal valence of O is always 2-, and the formal valence of V is 4+ for VO₂, 3+ for V₂O₃, and 2+ for VO, the effective charge of the VO₆ cluster is 8- for VO₂, 9- for V₂O₃, and 10- for VO. We also needed to specify the bond lengths/angles in the calculations because the electronic structure depends sensitively on the cluster geometry. To make our results realistic and useful, we used the same bond lengths/angles as those in the low-temperature single crystal of the corresponding compound. For example, to calculate the electronic structure of VO₂, we considered a VO₆ cluster with an effective charge of 8- and the coordinates of V and O atoms obtained from the low-temperature rutile VO₂ structure. We employed a commercial code, Dmol3, to perform first-principles electronic structure calculations for these clusters.

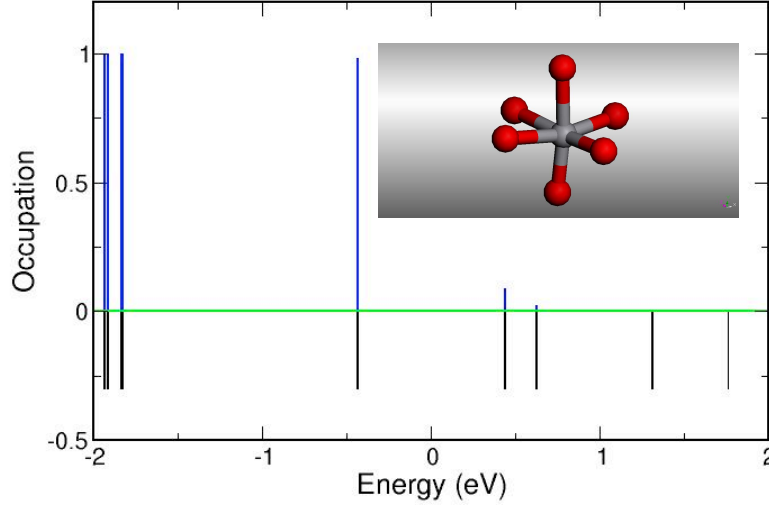


Figure 3 Electronic structure of a single cluster (VO_6)⁸⁻. Black bars represent individual energy levels, and the electron occupation of each energy level is represented by the height of the corresponding blue bar, with 1 being fully occupied and 0 being empty. The inset shows the coordinates of V (silver) and O (red) atoms in the cluster.

We calculated a VO_6 with an effective charge of 8- to mimic the polycrystalline VO_2 film. The coordinates of V and O atoms in the cluster were extracted from the low-temperature rutile VO_2 , and the structure was distorted with respect to a symmetric octahedron. The theoretical results are summarized in Fig. 3, which plots both the energy levels and their occupations. The HOMO and LUMO have the same spin orientation. The optical gap of this material should be the energy difference between the HOMO and LUMO, which is 0.9 eV—in good agreement with the gap of 0.86 eV inferred from experiment. In this structure, the HOMO is completely occupied, and the LUMO is completely unoccupied; in band language, the valence band is “full” and the conduction band is “empty.” Thus, there is no carrier in the system, and the transport activation energy in the semiconducting phase is used to create carriers.

c. Nonstoichiometric VO_x: charged double VO₆ clusters

As discussed above, when we changed the effective charge of a VO_6 cluster from 8- to 9-, the corresponding material changed from VO_2 to V_2O_3 . Because we could vary the charge only by an integer in this first-principles method, a single VO_6 cluster apparently was inadequate to describe VO_x with $1.5 < x < 2$. To overcome this limitation, we considered two adjacent VO_6 clusters instead of a single cluster. By varying the total charge of such a double cluster, we were able to study the electronic structures of $\text{VO}_{1.75}$, $\text{VO}_{1.25}$, and $\text{VO}_{0.75}$, among which $\text{VO}_{1.75}$ falls in the range of x values for microbolometers. In these double-cluster calculations, we set the bond lengths/angles to the values of a nearby stoichiometric compound. For example, to study the electronic structure of $\text{VO}_{1.75}$, we considered a few edge-sharing double clusters with an effective charge of 13- and coordinates of V and O atoms from the rutile VO_2 .

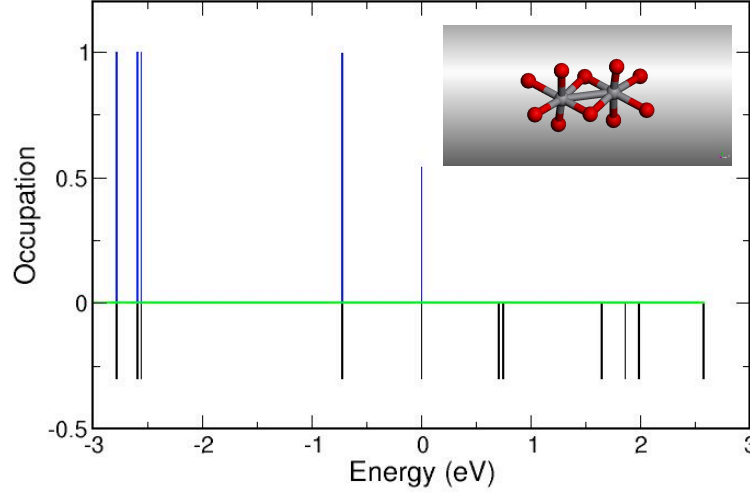


Figure 4 Electronic structure of the strongly coupled edge-sharing double cluster $(V_2O_{10})^{13-}$. The symbols are the same as those in Fig. 3. The inset shows the coordinates of V (silver) and O (red) atoms in the double cluster.

For the amorphous $VO_{1.8}$ film in Fig. 4., the formal valence of V is +3.6, which is not an integer. To study such a system with a fractional charge, we had to go beyond single cluster calculations. Here we considered a double edge-sharing VO_6 cluster with an effective charge of 13- to simulate $VO_{1.75}$, a compound sufficiently close to $VO_{1.8}$. Again, the coordinates of V and O atoms were obtained from the low-temperature rutile VO_2 . In VO_2 , there are two kinds of edge-sharing double VO_6 clusters., with one having a much shorter V-V distance (more strongly coupled) than the other. First, we focused on the strongly coupled double cluster. We found in this system that electrons at the two V atoms align their spins antiparallely. The introduction of an extra electron to the system, which changes the effective charge from 12- as in VO_2 to 13- as in $VO_{1.75}$, results in a drastically different electronic structure than that in Fig. 3. In the double cluster, as shown in Fig. 4, there is a doubly degenerate level at the Fermi level. These two degenerate levels have opposite spins and are both partially occupied. The degeneracy is easy to understand because the two V atoms have the opposite spin orientations, and the extra electron with spin either up or down would result in the same spin configuration. The optical absorption occurs when the electron in the two partially occupied states is excited to the next empty level, or when the electron in the highest fully occupied level is excited to these partially occupied states. The energy required is 0.7 eV for the former transition and 0.72 eV for the latter. Both the lowest empty and highest filled levels are doubly degenerate for up- and down-spin electrons, which guarantees that the optical transitions

d. Intercluster interactions

Calculating the electronic structure of a single or double VO_6 cluster gave us discrete energy levels. Those levels form energy bands when the wave function overlap (interaction) between adjacent clusters is taken into account. The bandwidth is proportional to the interaction and can be estimated by calculating the level splitting between adjacent clusters. For example, by comparing the results for VO_2 from the single cluster $(\text{VO}_6)^{8-}$ and weakly coupled double cluster $(\text{V}_2\text{O}_{10})^{12-}$ calculations, we deduced the interaction strength between clusters, which is half the energy splitting.

If the intercluster interaction is weaker than the on-site Coulomb interaction (Hubbard interaction), significant energy is required for an electron to hop to a singly occupied d -orbital, and the system is a Mott insulator. Otherwise, it is a metal or a Fermi liquid. When disorder is present, as in amorphous VO_x films, Anderson localization occurs. Therefore in VO_x films both Mott and Anderson localizations may be important to electrical transport.

We then calculated the electronic structure of the weakly coupled edge-sharing double clusters for $\text{VO}_{1.75}$ (see Fig. 5). We found that the electron spins at the two V atoms are parallel and that a small energy splitting, $W = 0.2$ eV, exists between the two levels near the Fermi energy. Because these levels belong to the same spin multiplets, optical transitions between these levels are forbidden do not occur. The splitting energy W characterizes the coupling ($t = W/2$) between the two V atoms in this double cluster, as well as the width of the energy band formed by these partially occupied states at different clusters. The small value of W suggests that the band is narrow and that these partially occupied states will become localized in the presence of even weak energy disorder, according to the Anderson localization theory, and that electric transport is through electron hopping between these partially occupied states. The transport activation energy is therefore the energy required for an electron located at one V atom to move to an adjacent V atom, i.e., the Coulomb energy between the hopping electron and the hole left behind,

$$E_a = e^2/\epsilon R \quad . \quad (1.1)$$

Here, ϵ is the dielectric constant of the material, and R ($= 3.12$ Å) is the distance between the two V atoms in this weakly coupled double cluster if we approximate ϵ in the $\text{VO}_{1.8}$ film with the value of VO_2 , which is 18.3 parallel to the tetragonal c -axis and 39 perpendicular to the axis. Because the transport activation energy should correspond to the largest energy required for electron hopping, we used the smaller dielectric constant $\epsilon = 18.3$ and find $E_a = 0.25$ eV.

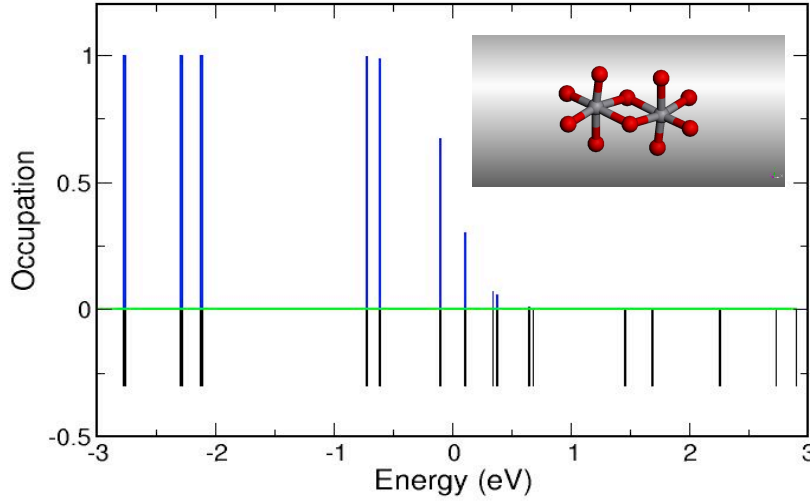


Figure 5 Electronic structure of the weakly coupled edge-sharing double cluster $(V_2O_{10})^{13-}$. The symbols are the same as those in Fig. 3. The inset shows the coordinates of V (silver) and O (red) atoms in the double cluster.

The agreement between this estimate and the experimental value, 0.3 eV is reasonably good. This activation energy is much larger than the coupling ($t = 0.1$ eV) between adjacent V-V atoms, which justifies neglecting the coupling in estimating the Coulomb energy. Because the distance R changes only slightly among various VO_x film, the transport activation energy is essentially determined by the dielectric constant, which generally increases with the carrier density. Thus we expected that as x is reduced, the dielectric constant would increase and the activation energy would decrease, which is what was observed experimentally. Moreover, 0.3 eV seems to be the maximal activation energy possible in VO_x if it has a Coulombic origin.

The optical absorption spectrum of the epitaxial $VO_{1.28}$ film suggests an optical gap of 0.2 eV in this system. Here we used the cluster calculations to identify its origin. We considered a double cluster with a certain effective charge to simulate $VO_{1.25}$. The coordinates of V and O atoms in such a cluster are extracted from the low-temperature corundum V_2O_3 structure. The corundum V_2O_3 structure has two kinds of adjacent double VO_6 clusters: one is face-sharing, and the other is edge-sharing. The effective charge is 13- for the former and 15- for the latter. We calculated both types of double clusters, and the results are summarized in Fig. 6. We found that in both clusters the electron spins at the V atoms are antiparallel and that doubly degenerate and partially occupied states appear at the Fermi level. The transition from the partially occupied states to the lowest empty states requires energy of 0.27 eV in the face-sharing double cluster and 0.32 eV in the edge-sharing one. The transition from the highest filled states to the partially occupied states requires energy of 0.93 eV in the face-sharing double cluster and 0.92 eV in the edge-sharing one. Thus the observed optical gap is due to the transition from the partially occupied states to the lowest empty states, and the calculated value of 0.27 eV explains the experimental value of 0.2 eV fairly well.

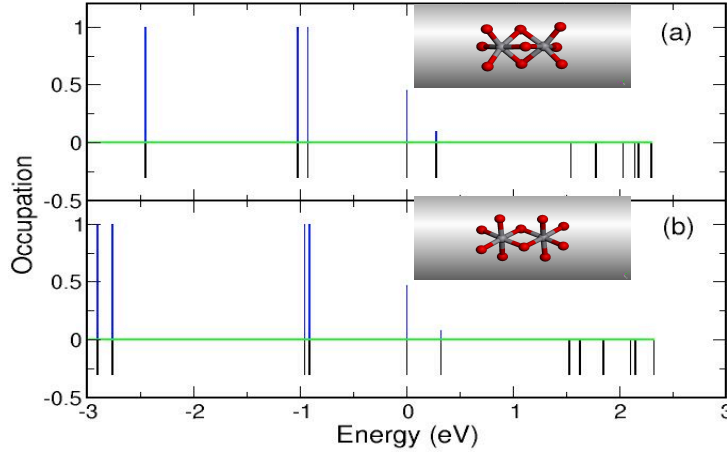


Figure 6 Electronic structure of the face-sharing double cluster $(V_2O_9)^{13-}$ (a) and the edge-sharing double cluster $(V_2O_{10})^{15-}$. The symbols are the same as those in Fig. 3. The insets show the coordinates of V (silver) and O (red) atoms in the corresponding double cluster.

2. ELECTRICAL TRANSPORT IN VOX

Because of the very localized d orbitals and large density of states in VO_x , we expected that the most probable hopping distance would be comparable to the lattice constant and that Mott's formula, which is based on a continuum model, might become inapplicable. To account for discrete hopping distances in VO_x , we considered a 3-dimensional (3D) cubic lattice, in which each site represents a V with a random energy and electrons can hop between any two lattice sites. Thus, variable-range hopping, if possible, is automatically included in the model. Here only t_{2g} orbitals are considered because the energy splitting between e_g and t_{2g} in VO_2 , according to the electron spin resonance experiment, is about 3 eV. We calculated the conductivity according to that definition.

2.1. DC CONDUCTIVITY

a. Model and approach

To describe the temperature-dependent conductivity in VO_x , we carried out a numerical calculation on a 3D cubic lattice, in which electrons can hop between any two sites. The hopping probability between sites i and j in the presence of an electric field \mathbf{E} can be written as

$$w_{ji} = w_{ij}^0 e^{-e\vec{E} \cdot \vec{R}_{ji} / k_B T}, \quad (2.1)$$

where $R_{ij} = |\vec{r}_i - \vec{r}_j|$ and w_{ij}^0 has the Miller-Abrahams form; i.e.,

$$w_{ij}^0 = \eta \exp(-2\alpha |R_{ij}|) \exp\left(\frac{\varepsilon(r_i) - \varepsilon(r_j)}{k_B T}\right) \quad \text{for } \varepsilon(r_i) < \varepsilon(r_j) \quad (2.2)$$

and

$$w_{ij}^0 = \eta \exp(-2\alpha |R_{ij}|) \quad \text{for } \varepsilon(r_i) > \varepsilon(r_j) \quad (2.3)$$

where $\varepsilon(r_i)$ is the carrier energy at site i , which follows some specified distribution. We solve the steady-state master equations for the system

$$0 = \sum_j [w_{ji} f_i (1 - f_j) - w_{ij} f_j (1 - f_i)], \quad (2.4)$$

where f_i is the carrier occupation number at site i . Having obtained the solution of f_i to Eq. (2.4), we can then calculate the current density,

$$J = \frac{e}{S} \sum_{i>s, j<s} [w_{ij} f_j (1 - f_i) - w_{ji} f_i (1 - f_j)], \quad (2.5)$$

where S is the cross-sectional area and $i > s, j < s$ denotes sites lying to the left and right of the cross section. The electrical conductivity σ can be obtained by $\sigma = J/E$.

In the linear-response regime, it has been shown that calculating conductivity is equivalent to finding an effective conductance of a random impedance network [8] in which each pair of sites, i and j , is connected by a resistance Z_{ij}

$$Z_{ij}^{-1} = (e^2 / k_B T) f_i^0 (1 - f_j^0) w_{ij}^0 = (e^2 / k_B T) f_j^0 (1 - f_i^0) w_{ji}^0 \quad (2.6)$$

where f_i^0 is the equilibrium occupation of site i , $f_i^0 = \frac{1}{1 + e^{[\varepsilon(r_i) - \mu]/k_B T}}$.

To calculate the effective conductance of this impedance network, imagine that two contacts are attached to two opposite surfaces of the lattice through which a constant current I is supplied. The effective conductance G can be obtained by calculating the voltage drop V between the two contacts, $G = I/V$. In the calculations a very large hopping probability between a contact and the lattice surface to which the contact is attached was used, which meant that the interfacial resistance between the contacts and the lattice is very small. The results are insensitive to the specific value of hopping probability assumed between the contact and the lattice surface and the system size.

Our numerical results and the experimental data were in excellent agreement when the energy disorder follows a uniform distribution between $[-\Delta, \Delta]$ with $\Delta = 0.54$ eV and the wave-function delocalization parameter is set $\alpha = 3.9 \text{ \AA}^{-1}$ (the lattice constant is fixed $a = 3 \text{ \AA}$), as shown in Fig. 7. Our model accounts for crossover of the conductivity with decreasing temperature. Above the crossover temperature, the conductivity has an activated behavior, whereas below that temperature, the conductivity has a weaker temperature dependence and can be fitted into $\exp(-(T_0/T)^{1/4})$ behavior. The activated behavior occurs when electrons hop only between the nearest-neighboring sites in the lattice.

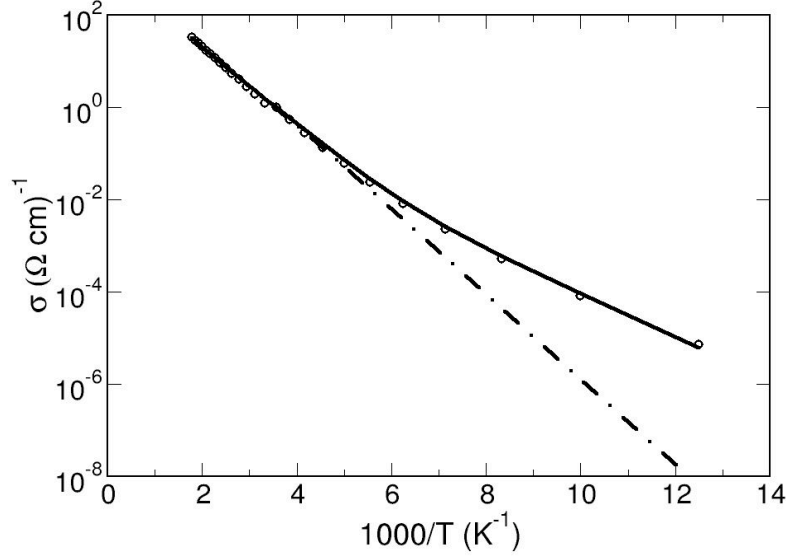


Figure 7. Logarithm of conductivity σ versus inverse temperature. Circles are experimental data from De Wames's group. The solid line shows the results of our model using a uniform energy distribution $[-\Delta, \Delta]$ with $\Delta = 0.54$ eV and $\alpha = 3.9$ Å⁻¹. The dot-dashed line shows the results of a system where electrons can hop only to the nearest neighbors.

In this lattice model, we assumed that every site contains one electronic state for transport and thus the density of the states is $1/2a^3\Delta = 3.4 \times 10^{22}$ 1/(cm³ eV). We also assumed that every electronic state in the model is localized, which is reasonable because the disorder 2Δ is much greater than the bandwidth in an ordered stoichiometric VO_x (~ 0.1 eV). In a one-dimensional disordered system, it has been shown that $\alpha a \approx 0.1142(\Delta/t_0)^2$ [E.N. Economou, *Green's Functions in Quantum Physics*, Springer-Verlag, Berlin, 1983], where t_0 is the transfer integral of the adjacent atom (half of the band width in 1d). If Δ/t_0 is 10, α would be 3.8 Å⁻¹, close to the value in the numerical calculations.

The ratio, $\alpha^3/k_B N(E_F)$, in the numerical calculations is 2.0×10^7 (K), and $T_0/[\alpha^3/k_B N(E_F)] = 18$, which is twice as large as 7.6 from the original Mott's formula, but is in the middle of the range, $2.5^4 - 1.7^4$, among various treatments. The most probable hopping distance is $R = (3/8\alpha)(T_0/T)^{1/4}$, which corresponds to 3.19 Å at $T = 300$ K and 4.4 Å at $T = 80$ K.

We developed several codes using different algorithms and/or boundary conditions to compute the electrical conductivity in VO_x. These codes not only ensure the reliability and accuracy of our numerical results but also provide efficient options for different situations. For example, when the disorder is strong and the carrier hopping distance is considerably shorter than the system size, the code using the sparse-matrix technique will be more effective.

b. Extension of Mott's variable range hopping theory

The variable-range-hopping theory by Mott is probably the most important and original theory to describe electrical transport in disordered systems and won Mott the Nobel Prize in physics in 1977. In the course of computing the electrical conductivity in VO_x and explaining the experiments, we found that the original variable-range-hopping theory can be extended.

Mott's theory makes two assumptions: (1) the average hopping distance is much greater than the lattice constant, and continuum expressions are justified; and (2) the hopping distance has a very narrow distribution (δ -function like) and a single “most probable hopping distance” can describe electron hopping accurately.

Figure 8 shows the distribution of hopping distance from our simulations, which is defined by

$$D(R^2) \equiv \frac{\sum_{i \neq j} |I_{ij}(R_{ij}^2 = R^2)|}{\sum_{i \neq j} |I_{ij}|} . \quad (2.7)$$

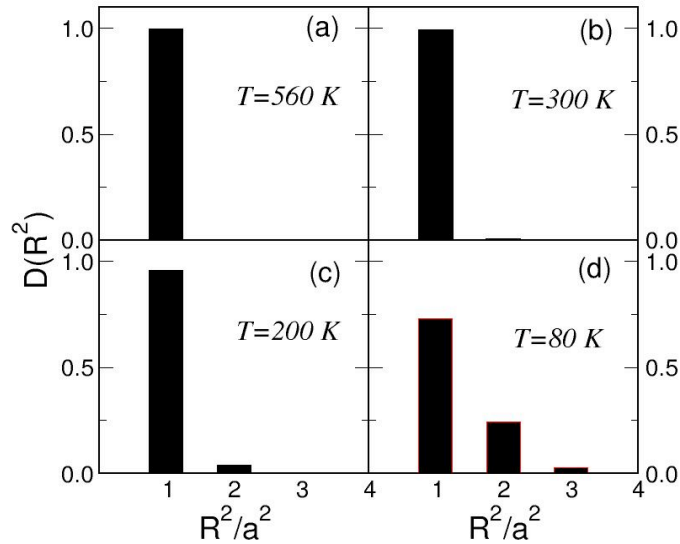


Figure 8 Histograms showing the distribution of hopping distances at several temperatures.

Here I_{ij} is the current through the resistance Z_{ij} between sites i and j of the impedance network. For the parameters used in Fig. 7, hopping to the nearest neighbors ($R^2/a^2 = 1$) is always dominant. As the temperature decreases, next-nearest-neighbor hopping becomes more and more important. The contribution from hopping beyond next nearest neighbors ($R^2/a^2 \geq 3$) is negligible. Thus, the variable-range hopping here means that electrons can hop either to the nearest neighbors or to the next-nearest neighbors, which are not much farther than the lattice constant. If a single “most probable hopping distance” did exist, as assumed in Mott's theory, it would be the nearest neighbor ($R = a$), and the temperature dependence of conductivity would always have an activated behavior, as shown by the dot-dashed line in Fig. 7. It is obvious that Mott's theory is not applicable to this situation.

2.2 AC ELECTRICAL TRANSPORT IN VOX

AC conductivity measurements can provide information about the transport mechanism and the absolute value of hopping frequency and become particularly important in characterizing electric transport in strongly disordered systems, where the Hall effect and magnetoresistance measurements do not yield as much useful information as do crystalline semiconductors. To support the MURI team's experimental efforts in characterizing electric transport in VO_x and α -Si, we augmented our original proposal with tasks to develop modeling tools for AC conductivity and thermopower calculations.

a. Impedance network

To calculate the AC conductivity in a disordered system like VO_x, we studied the master equation in the linear approximation with respect to an external AC electrical field,

$$\vec{E}(t) = \vec{E} \exp(i\omega t), \quad (2.8)$$

where ω is the field frequency. The time-dependent master equation for a disorder system in a 3D lattice reads

$$\frac{df_m}{dt} = \sum_n [f_n(1 - f_m)w_{mn} - f_m(1 - f_n)w_{nm}], \quad (2.9)$$

where f_m is the electron occupation on site m , and w_{nm} is the electronic hopping rate from site m to site n in the presence of the external field. The general solution to the master equation can be written as

$$f_m(t) = f_m^0 + \delta f_m e^{i\omega t}, \quad (2.10)$$

where f_m^0 is the equilibrium occupation at site m , determined by the Fermi-Dirac distribution,

$$f_m^0 = [1 + \exp(\epsilon_m - \mu)/k_B T]^{-1}, \quad (2.11)$$

with a common chemical potential (Fermi level) μ across the system. In the presence of an AC electric field, the occupation changes, which can be attributed to a shift in local chemical potential, $\delta\mu_m$,

$$\delta f_m = \beta \delta\mu_m f_m^0 (1 - f_m^0). \quad (2.12)$$

If we expand δf_m in terms of the applied field, and keep only the linear terms of \mathbf{E} , the master equation can be written as

$$i\omega C_m(U_m + \mathbf{E} \cdot \mathbf{R}_m) = \sum_{m'} (U_{m'} - U_m)/Z_{m'm}, \quad (2.13)$$

where \mathbf{R}_m is the position vector of site m , and

$$U_m = -\mathbf{E} \cdot \mathbf{R}_m + \delta\mu_m/e$$

$$Z_{mn}^{-1} = \frac{e^2}{k_B T} f_m^0 (1 - f_n^0) w_{nm}^0 = \frac{e^2}{k_B T} f_n^0 (1 - f_m^0) w_{mn}^0,$$

$$C_m = \frac{e^2}{k_B T} f_m^0 (1 - f_m^0)$$

Hence the calculation of AC conductivity is reduced to finding an effective conductance of a random impedance network at frequency ω . In this network every two sites m and n are connected by a resistance Z_{mn} , and each site m is attached with a capacitance C_m and a source of voltage $-\mathbf{E} \cdot \mathbf{R}_m$. We numerically solve the linear equations (2.13) with complex coefficients to compute the effective conductance.

If valence electrons are highly localized, as in VO_x films used in microbolometers, possible electron hoppings are limited to sites in a few near neighboring sites. Consequently, the matrix in Eq. (2.13) will be sparse, which allows study of a large system using sparse-matrix techniques. However, the matrix is both complex and asymmetric, and the commonly used conjugated gradient method for a symmetric matrix does not work in this case. We used a generalized minimum residual method, which works for asymmetric matrices, to solve Eq. (2.13), and the system size in our calculations is $32 \times 32 \times 32$ sites.

b. Numerical results

We considered a cubic lattice with $32 \times 32 \times 32$ sites in the presence of energy disorder and calculated its AC conductivity with different field frequencies. The hopping probability between sites i and j has the Miller- Abrahams form; i.e.,

$$w_{ij}^0 = v \exp(-2\alpha |R_{ij}|) \exp\left(\frac{\varepsilon(r_i) - \varepsilon(r_j)}{k_B T}\right) \quad \text{for } \varepsilon(r_i) < \varepsilon(r_j),$$

and

$$w_{ij}^0 = v \exp(-2\alpha |R_{ij}|) \quad \text{for } \varepsilon(r_i) > \varepsilon(r_j),$$

where $\varepsilon(r_i)$ is the carrier energy at site i , and $R_{ij} = |\vec{r}_i - \vec{r}_j|$ is the distance between sites i and j . Here v determines the hopping frequency and is usually believed to be comparable to the optical phonon frequency of the system. We expect that by varying the interplay of v and the AC field frequency ω , the transport behavior will change.

Figure 9 plots the conductivity versus logarithm of ω/ν at room temperature. The site energy is assumed to follow a uniform distribution between $[-\Delta, \Delta]$, and the lattice constant is $a = 3 \text{ \AA}$ and the wave function localization parameter is $\alpha = 3 \text{ \AA}^{-1}$. A steep increase occurs in the AC conductivity around $\omega/\nu = 10^{-8}$, before (low-frequency) and after (high-frequency), which the conductivity is largely independent of ω . Because the typical hopping probability is $\nu \exp(-2\alpha a)$, which is about $1.5 \times 10^{-8} \nu$ for the parameters we used, the conductivity jump occurs when the AC frequency is similar to the electron hopping frequency. This steep change in conductivity with varying field frequencies allows determination of the absolute value of ν , which is important for establishing a quantitative and predictive electric transport model.

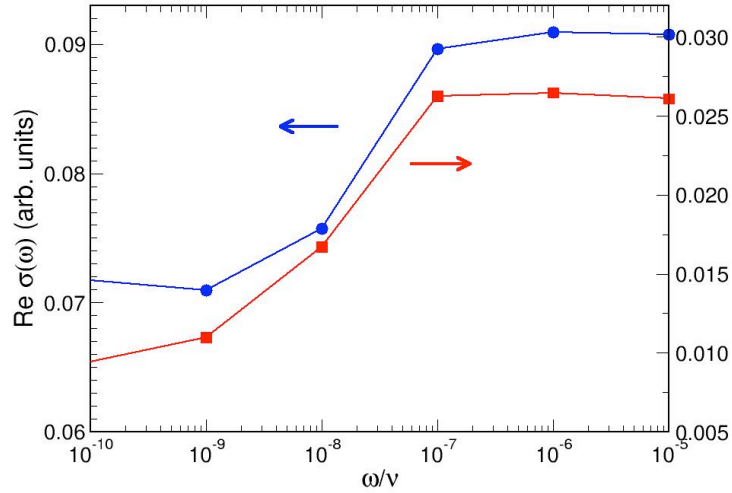


Figure 9. Real part of conductivity as a function of ω/ν in a $32 \times 32 \times 32$ cubic lattice with energy disorder. Circles and squares correspond to $\Delta = 0.1$ and 0.2 eV, respectively. Other parameters are $\alpha = 3 \text{ \AA}^{-1}$ and $a = 3 \text{ \AA}$.

Figure 10 plots the temperature dependence of AC conductivity for different field frequencies. Solid, dashed, and dot-dashed lines describe results with $\omega/\nu = 10^{-10}$, 10^{-8} , and 10^{-3} , which belong, respectively, to the low-frequency, crossover, and high-frequency regimes illustrated in Fig. 9. Conductivity increases with frequency, and the increase is more pronounced at low temperatures than at high temperatures. The conductivity increase is a consequence of the disorder: with increasing frequency, during half a period of the external field, charge carriers can move through clusters of decreasing size. Thus with an increase of frequency, well-conducting regions of finite size become more and more effective. At high temperatures electron hopping is essentially limited to nearest neighbors, and a high field frequency cannot further reduce the electron moving distance. Consequently, the conductivity increase is not significant at higher temperatures.

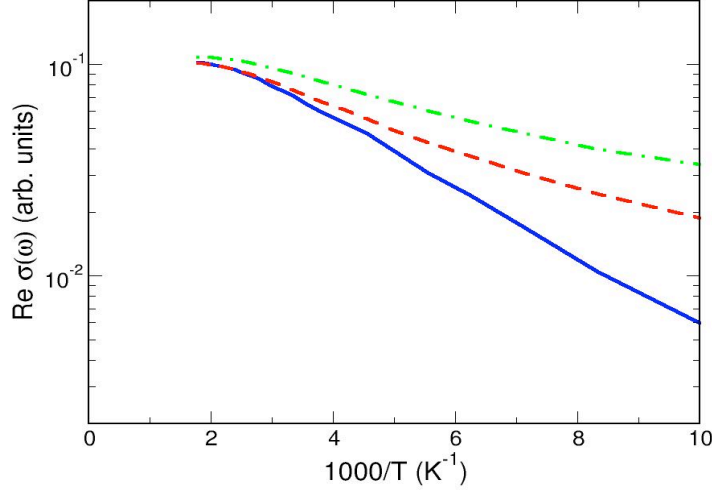


Figure 10. Real part of conductivity as a function of inverse temperature in a $32 \times 32 \times 32$ cubic lattice with energy disorder. Solid, dashed, and dot-dashed lines correspond to $\omega/v = 10^{-10}$, 10^{-8} , and 10^{-3} , respectively. Other parameters are $\alpha = 3 \text{ \AA}^{-1}$, $a = 3 \text{ \AA}$ and $\Delta = 0.1 \text{ eV}$.

2.3 THERMAL POWER IN VO_x

The thermal power in a disordered system provides information about the sign of the charge of the majority carriers and the Fermi level position, and helps identify the transport mechanism in materials. In addition it offers a good opportunity to test theoretical models because it is sensitive to material parameters.

Thermal power can be calculated by two ways: (1) finding the current density in the presence of a temperature gradient and then determining the thermal power by requiring zero total current and a uniform chemical potential; and (2) calculating the energy flux in the absence of a temperature gradient and finding the Peltier heat, which is the product of the temperature and the thermal power. We used the latter approach.

We solve the steady-state master equations for the system in the presence of an applied electric field,

$$0 = \sum_n [w_{mn} f_m (1 - f_n) - w_{nm} f_n (1 - f_m)]. \quad (2.14)$$

Having obtained the solution of f_m , we then calculate the charge flux (current) across a plane normal to the electric field,

$$I = e \sum_{m < s, n > s} [w_{mn} f_m (1 - f_n) - w_{nm} f_n (1 - f_m)], \quad (2.15)$$

where $m < s$, $n > s$ denotes sites lying to the left and right of the cross section, and e is the absolute value of the electron charge. Similarly, we calculate the energy flux

$$q = \sum_{m < s, n > s} \frac{1}{2} (\varepsilon_m + \varepsilon_n) [w_{mn} f_m (1 - f_n) - w_{nm} f_n (1 - f_m)], \quad (2.16)$$

where ε_m is the electron energy at site m . The Peltier heat can be obtained by

$$\Pi = \frac{e}{I} q - \mu, \quad (2.17)$$

where μ is the common Fermi energy throughout the system, and the Seebeck thermal power is

$$S = \Pi / eT. \quad (2.18)$$

If valence electrons are highly localized, as in VO_x films used in microbolometers, possible electron hoppings are limited to sites within a few near neighboring sites. Consequently, the matrix in Eq. (2.14) will be sparse, which allows study of a large system using sparse-matrix techniques. We used a generalized minimum residual method, which works for both symmetric and asymmetric matrices, to solve Eq. (2.14).

Figure 11 plots the thermal power as a function of temperature. The site energy is assumed to follow a uniform distribution between $[-\Delta, \Delta]$, and the lattice constant is $a = 3 \text{ \AA}$ and the wave function localization parameter is $\alpha = 3 \text{ \AA}^{-1}$. At low temperatures, the thermal power is negative with a large magnitude, whereas at high temperatures it is positive with a small magnitude. A positive (negative) thermal power indicates that on average the carrier energies are above (below) the Fermi level. Hence the calculated results suggest that at low temperatures the carriers responsible for transport are mainly localized below the Fermi level. As temperature increases, these carriers move toward the Fermi level and eventually surpass it. At high temperatures, these carriers essentially dwell on the Fermi level.

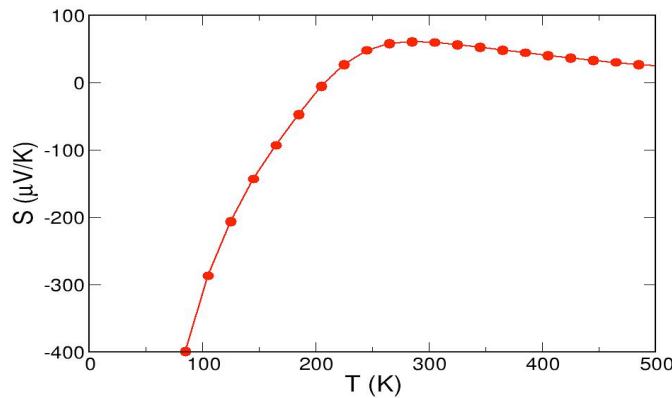


Figure 11 Thermal power as a function of temperature in a $32 \times 32 \times 32$ cubic lattice with energy disorder. Other parameters are $\alpha = 3 \text{ \AA}^{-1}$, $a = 3 \text{ \AA}$ and $\Delta = 0.4 \text{ eV}$.

3. MICROSTRUCTURES IN VO_x AND THEIR SIGNATURES IN LINEAR TRANSPORT

The MURI team led by Prof. Mark Horn from Penn State, which has extensively studied structural and transport properties of VO_x samples grown under various conditions, has found that microstructures or nanocrystals are ubiquitous in VO_x thin films. However, it is unclear how these microstructures affect electrical transport. For example, samples with multiple microstructures can have a very similar DC conductivity and temperature dependence, compared with truly amorphous samples with few microstructures.

Because these microstructures are a main source of the noise that limits performance of microbolometers, it is important to identify their experimental signatures and to study how they affect transport properties. According to our modeling results on nonlinear conductivity in VO_x, one of the signatures is nonlinear electrical conductivity under a strong electric field.

3.1 DESCRIPTION OF MICROSTRUCTURES

To model how the microstructures or nanocrystals influence electrical transport in VO_x and other disordered systems, the microstructures need to be described quantitatively, but at the same time their essential physics also need to be determined. To this end, we noticed that within these microstructures the electronic structure is similar to that in a crystal; however, for a length scale larger than the size of the microstructures, the electronic structure exhibits the characteristics of a disordered system. We incorporated these structural effects by introducing a spatial correlation between electron energies at different sites, with the correlation length being the microstructure size. A representative correlation can be written as

$$\langle \varepsilon_i \varepsilon_j \rangle = \frac{\Delta^2 a}{R_{ij}} e^{-R_{ij}/L} \quad (3.1)$$

Here ε_i is the electron energy (random variable) on site i , $R_{ij} = |\mathbf{r}_i - \mathbf{r}_j|$ is the distance between sites i and j (\mathbf{r}_i is the location of site i), and L is the correlation length. Spatially correlated disorder is not unique in VO_x and has been cited to explain both electron and energy transport in various disordered systems.

Because common numerical tools can generate only independent (uncorrelated) random numbers, to numerically generate spatially correlated energy disorder that satisfies the correlation function of Eq. (3.1), finding a new “space” where the correlated disorder becomes decoupled is necessary. We noticed that in the momentum space the disorder becomes decoupled among different momentum \mathbf{q} as clearly seen when ε_i is substituted by its Fourier transform,

$$\varepsilon_i = \frac{1}{N} \sum_{\mathbf{q}} \Phi(\mathbf{q}) e^{i\mathbf{q} \cdot \mathbf{r}_i} \quad (3.2)$$

where N is the total number of lattice sites. Equation (3.1) then becomes

$$\langle |\Phi(\mathbf{q})|^2 \rangle = \Delta^2 \frac{1}{\mathbf{q}^2 + L^{-2}}. \quad (3.3)$$

Thus in the momentum space the energy disorder $\Phi(\mathbf{q})$ for different \mathbf{q} becomes decoupled and has a \mathbf{q} -dependent variance. For the cubic lattice we used to study transport, \mathbf{q} has only discrete values. We generated a random $\Phi(\mathbf{q})$ from a Gaussian distribution with the \mathbf{q} -dependent variance as in Eq. (3.3) for each and every \mathbf{q} . Then we Fourier-transformed the obtained $\Phi(\mathbf{q})$, according to Eq. (3.2), back to ε_i , which would have the desired spatial correlation. Figure 12 shows the spatial correlation in the random site energies generated by this approach.

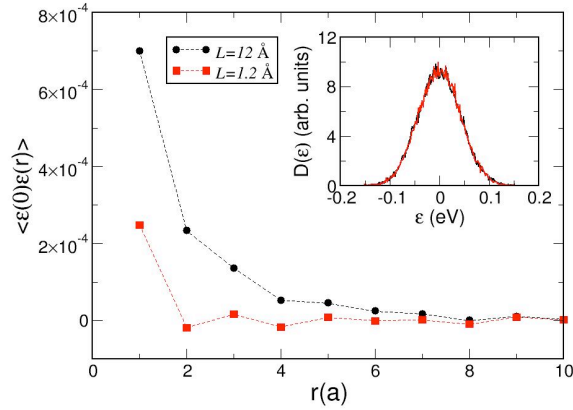


Figure 12 Spatial correlation of numerically generated random electron energies in the lattice. Circles and squares correspond to $L = 12$ and 1.2 \AA , respectively. The inset plots the distribution of electron energies, which shows a same variance for the two cases.

3.2 EFFECT OF MICROSTRUCTURE ON TRANSPORT

We examined how the domain size, or equivalently, the correlation length, L , influences the transport behavior in VO_x films. Figure 13 shows conductivity and thermal power as functions of temperature for systems with different correlation lengths. As correlation length increases, conductivity also increases, while the overall temperature dependence of the conductivity changes little. However, the temperature dependence of the thermal power can change dramatically as the domain size changes. These results suggest that the thermal power measurements provide information about the microstructures of VO_x films, which is particularly important in microbolometers because the microstructures are likely to determine operation speed and noise level.

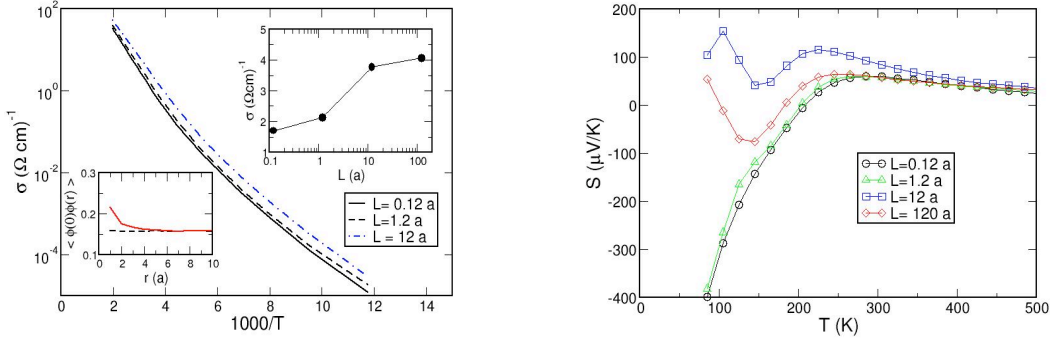


Figure 13. Conductivity and thermal power as a function of inverse temperature in a 32x32x32 cubic lattice with different correlation lengths. Other parameters are the same as those as in Fig. 12.

4. DYNAMICS OF DEFECT MICROSTRUCTURES

Bulk nonstoichiometric vanadium oxides, which often conform to the generic formula, $\text{V}_n\text{O}_{2n-1}$, are also called Magneli phases. Crystalline Magneli phases have large unit cells, especially when n is large. A thin amorphous film of VO_x , the material form used for an uncooled bolometer, however, is unlikely to accommodate the large unit cells of the Magneli phases, which suggests that the ordered Magneli phases are probably unimportant to a VO_x film.

Because the Magneli phases are defined by the general stoichiometric formula, $\text{V}_n\text{O}_{2n-1} = \text{V}_2\text{O}_3 + (n-2)\text{VO}_2$, and can be regarded as a mixture of VO_2 and V_2O_3 , an amorphous VO_x film should consist of many domains of VO_2 or V_2O_3 , and the distribution of these domains should be temperature-dependent.

We have developed a model to describe the dynamics of these domains when the system is subjected to an abrupt temperature change. The dynamics of these microstructures are important for bolometer applications because they determine how fast the system can respond to a temperature change and may be the source of the inconvenient image retention during the device operation.

The chemical-potential difference $\Delta\mu$ of VO_2 and V_2O_3 differs because of their different densities,

$$\Delta\mu = -(3/2) k_B T \log (m_1/m_2), \quad (4.1)$$

where m_1 and m_2 are densities of VO_2 and V_2O_3 . The average size of domains can be estimated by the balance between the volume energy gain and the surface energy cost. If we assume that the domains are spheres, the free energy of a domain is

$$F = -4\pi(\Delta\mu)L^3/3 + 4\pi sL^2, \quad (4.2)$$

where s is the surface energy for a unit area. By requiring $\delta F/\delta L = 0$, we have

$$L = 2 s/(\Delta\mu). \quad (4.3)$$

Thus, the average domain size becomes smaller as the temperature increases. If the system temperature suddenly drops, as it does when a strong IR signal arrives, the domains adjust their sizes to reach equilibrium at a lower temperature. The diffusion current should be proportional to the gradient of the chemical potential difference,

$$J \propto \nabla\mu \approx \Delta\mu/L \propto 1/L^2 \quad (4.4)$$

On the other hand, the diffusion current is the consequence of change in the domain size, $J \propto dL/dt$.

Hence the time-evolution of L should follow

$$dL/dt \propto 1/L^2 \quad (4.5)$$

and we obtain a generic behavior of $L(t)$

$$L(t) \sim t^{1/3}. \quad (4.6)$$

This time dependence of the domain size implies that the resistance will slowly decay to its equilibrium value with the following form,

$$\Delta R/R_0 \propto \exp [-(t/\tau)^{1/3}], \quad (4.7)$$

after the system receives a large current signal. This theory explains the observed long-tail decay of the resistance after the system is subjected to a large current pulse. The dynamics of the microstructures may be the source of image retention—a serious problem that adversely affects the sensitivity of VO_x-based microbolometers.

5 DISTINCT ELECTRICAL TRANSPORT MECHANISMS IN VO_x AND α -Si:H

In developing models to understand electrical transport in VO_x, we found that the conductivity in VO_{1.8} can be quantitatively explained by electron hopping among localized d states, and that the crossover is due to the transition from long-range hoppings at low temperatures to strictly nearest-neighbor hoppings at high temperatures. This mechanism suggests that VO_x differs markedly from many conventional disordered semiconductors such as α -Si, whose properties are cited in the literature. To demonstrate that VO_x indeed has a unique transport mechanism, we analyzed transport data of hydrogenated α -Si measured by Dr. A. J. Syllaos and compared them with those of VO_x.

Figure 14 shows the measured electrical conductivity of a VO_x film as a function of $1000/T$ for temperatures from 80 to 560 K. A crossover in conduction behavior occurs at $T = 300$ K. For $T > 300$ K, the electrical conductivity data can be described by the Arrhenius formula, $\sigma_h(T) = \sigma_h^0 \exp(-E_a/k_B T)$, where $E_a = 0.182$ eV and $\sigma_h^0 = 1.4 \times 10^3 (\Omega \text{ cm})^{-1}$. For $T < 300$ K, the conductivity is described by Mott's 1/4-law for variable-range hopping $\sigma_l(T) = \sigma_l^0(T) \exp[-(T_0/T)^{1/4}]$, where the prefactor $\sigma_l^0(T) = 7.91 \times 10^{15}/T^{1/2}$ and $T_0 = 3.66 \times 10^8$ K. Of note, the value of σ_h^0 is identical to the observed minimum metallic conductivity in VO_x.

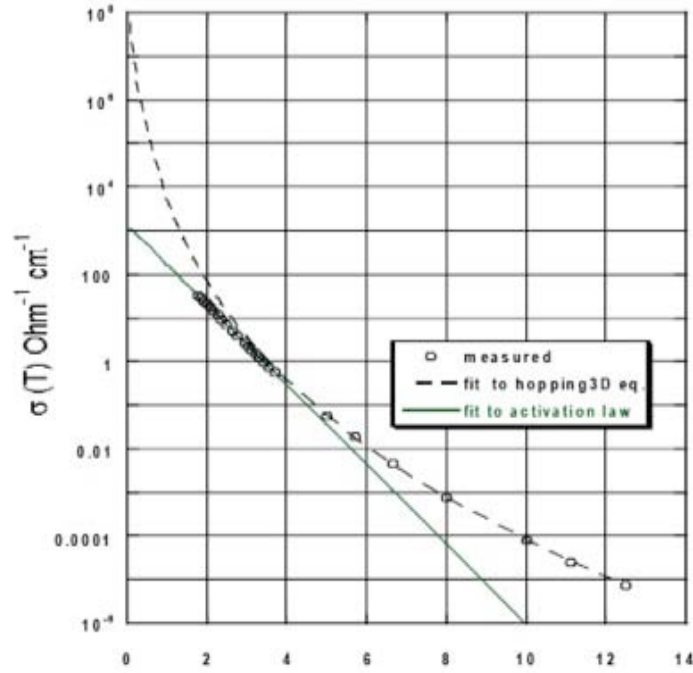


Figure 14. Logarithm of electrical conductivity for an unsuspended 16x16 mm² VO_x film as a function of inverse temperature.

Figure 15 shows the measured temperature-dependent conductivity in the α -Si:H thin film. The conductivity can also be fitted by $\sigma_h(T) = \sigma_h^0 \exp(-E_a/k_B T)$, with $E_a = 0.226$ eV and $\sigma_h^0 = 38.98 (\Omega\text{cm})^{-1}$ for $T > 250$ K; and $\sigma_l(T) = \sigma_l^0 \exp[-(T_0/T)^{1/4}]$, with $\sigma_l^0(T) = 1.64 \times 10^6$ and $T_0 = 5.57 \times 10^7$ K for $T < 200$ K. Although the transport data for VO_x and α -Si:H appear to be similar, close scrutiny reveals a significant difference. In α -Si:H, the total conductivity for the entire measured temperature range can be described by the summation of the two contributions,

$$\sigma(T) = \sigma_l(T) + \sigma_h(T), \quad (5.1)$$

with $\sigma_l(T)$ dominating at low temperatures and $\sigma_h(T)$ at high temperatures. Thus, electron conduction in α -Si has two parallel channels: one is the thermal activation of electrons from localized impurity states to the extended conduction band; the other is hopping among localized states in the impurity band. The two-channel model also describes electrical transport in chalcogenide glass and other disordered semiconductors.

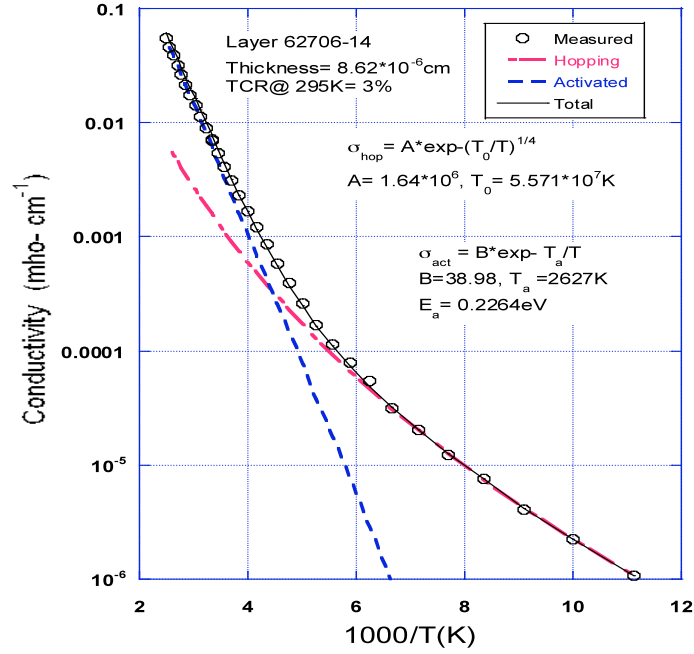


Figure 15 Logarithm of electrical conductivity for an unsuspended α -Si:H film as a function of inverse temperature.

with $\sigma_l(T)$ dominating at low temperatures and $\sigma_h(T)$ at high temperatures. Thus, electron conduction in α -Si has two parallel channels: one is the thermal activation of electrons from localized impurity states to the extended conduction band; the other is hopping among localized states in the impurity band. The two-channel model also describes electrical transport in chalcogenide glass and other disordered semiconductors.

In VO_x , however, such a two-channel model does not fit the transport data of $\text{VO}_{1.8}$. If the fitted expression $\sigma_l(T) = \sigma_l^0(T) \exp[-(T_0/T)^{1/4}]$ is extrapolated to $T > 300$ K, as shown in Fig. 15, it would be greater than the measured conductivity $\sigma(T)$. Hence, the data suggest that at high temperatures variable-range hopping becomes unavailable to electrons.

The distinct transport mechanisms in VO_x and α -Si originate from their fundamental differences in electronic structure. In VO_x the valence electrons are from very localized $3d$ orbitals, whereas in α -Si the valence electrons are from delocalized $3s$ and $3p$ orbitals. In addition, amorphous VO_x is a heavily defective oxide, and the origin of the disorder is in the compositional variation due to variable cation valence. For $x = 1.8$, roughly 40% of V ions have a valence of $3+$ ($3d^2$), as in V_2O_3 , and the remaining 60% have a valence of $4+$ ($3d^1$), as in VO_2 . The weak bonding between d orbitals makes them susceptible to disorder; they become localized due to structural and composition disorders in amorphous VO_x via Anderson localization. Thus, it is reasonable to assume that VO_x is a Fermi glass with $3d$ orbitals at each V atom randomly distributed, and that electron conduction in this band takes place only via hopping between individual localized states. This assumption is corroborated because σ_h^0 , the extrapolated value of $\sigma_h(T)$ as $T \rightarrow \infty$, is the same as the minimum metallic conductivity, which is obtained when the carrier mean free path becomes equal to the lattice constant. The different transport mechanisms in VO_x and in α -Si:H are illustrated in Fig. 16.

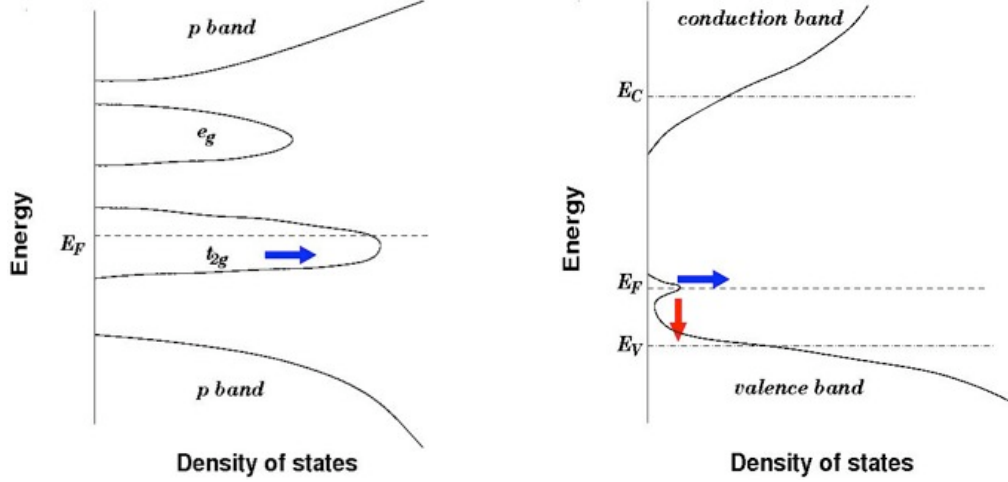


Figure 16 Schematic diagrams showing the electronic structure and conduction paths in VO_x (left panel) and $\alpha\text{-Si:H}$ (right panel). In VO_x the Fermi energy E_F is located in the t_{2g} band and the conduction is due to electron hopping between localized states in the t_{2g} band, as denoted by the blue arrow. In $\alpha\text{-Si:H}$ the Fermi energy E_F is located at the valence-band tail. E_C and E_V are the mobility edge in the conduction and valence bands, respectively. Both carrier hopping between localized states (denoted by blue arrow) and excitation to the mobility edge (denoted by red arrow) contribute to the total conductivity. The excitation energy extracted from $\sigma_h(T)$ corresponds to $E_a = E_F - E_V$.

6. ELECTRICAL CONDUCTIVITY AT HIGH ELECTRIC FIELDS AND THE EFFECT OF MICROSTRUCTURES

6.1 Model and algorithm

To quantitatively study high-field electrical transport in VO_x and the manifestation of microstructures in nonlinear transport, we developed a versatile lattice model to calculate the conductivity of a disordered system. We began with the same 3D cubic lattice in which electrons can hop between any two lattice sites thereby automatically including variable-range hopping in the model. An applied electric field, \mathbf{E} , tilts the energy difference between sites i and j

$$\varepsilon(r_i) - \varepsilon(r_j) \rightarrow \varepsilon(r_i) - \varepsilon(r_j) - e\mathbf{E} \cdot \mathbf{R}_{ji}, \quad (6.1)$$

and the hopping probability becomes

$$w_{ij} = \eta \exp(-2\alpha|R_{ij}|) \exp\left(\frac{\varepsilon(r_i) - \varepsilon(r_j) - e\mathbf{E} \cdot \mathbf{R}_{ji}}{2k_B T}\right). \quad (6.2)$$

To study high-field electrical transport, we needed to solve the steady-state master equations,

$$0 = \sum_j [w_{ji} f_i (1 - f_j) - w_{ij} f_j (1 - f_i)], \quad (6.3)$$

in the presence of a strong electric field, \mathbf{E} . These equations are nonlinear, and solving them is a significant numerical challenge. On the other hand, for electrical transport under a weak field, Eq. (6.3) can be linearized, with *linear* equations solved to compute the electrical conductivity.

We developed an iteration approach to solve these nonlinear equations accurately. From the master equation (6.3), we express f_i as

$$f_i = \frac{\sum_j w_{ij} f_j}{\sum_k w_{ki}} \left[1 - \frac{\sum_j (w_{ji} - w_{ij}) f_j}{\sum_k w_{ki}} \right]^{-1}. \quad (6.4)$$

In Eq. (6.4), we scaled all hopping rates by $\sum_k w_{ki}$ to avoid very large or small numbers. Using the above equation, we updated f_i using *implicit* iterations until the accuracy criterion was satisfied. Specifically, if we obtain f_i^{n-1} ($1 < i < N$, N is the total number of the lattice sites), as the solution after step $n-1$, then to calculate f_i at the next step (n), in the right-hand side of the above equation we used f_j^n for $j < i$ and f_j^{n-1} for $j > i$. We found that if we used *explicit* iteration (i.e., f_j^{n-1} for all j), the iteration scheme did not converge.

Figure 17 describes the effect of correlated energy disorder on the electrical conductivity, plotting conductivity at field E and temperature T , $\sigma(E, T)$, normalized by the low-field conductivity at temperature T , $\sigma(T)$, as a function of E for two correlation lengths. For $L = 1.2 \text{ \AA}$, which is much smaller than the lattice constant a , the electron energies at different sites are essentially independent (uncorrelated). For $L = 12 \text{ \AA}$, the spatial correlation extends to a few lattice constants, and the electron energies, although still random, tend to be closer to each other for vicinal sites.

Figure 17 shows that when the energy disorder is not spatially correlated, as described by the triangles; the field dependence is very weak, and consequently a much higher electric field is required for the sizable deviation of $\sigma(E, T)$ from $\sigma(T)$, which is not consistent with the experiment data in Fig. 18. When the electron energies are spatially correlated, as described by the squares, $\sigma(E, T)$ starts to deviate significantly from $\sigma(T)$ around 10^4 V/cm , as observed experimentally.

Our results suggest that to understand the strong nonlinear conductivity observed in VO_x , the spatial correlation in electron energies must be taken into account. This spatial correlation originates from microstructures (domains) and nanocrystals in VO_x films. Our numerical results also indicate that the spatial correlation manifests itself in the field dependence of conductivity, but remains hidden in the temperature dependence of conductivity.

7. MODELING $1/f$ NOISE

Currently, microbolometer performance is limited by $1/f$ noise and image retention, which are likely to originate from nonequilibrium kinetic processes with a broad distribution of relaxation times. Understanding the noise origin is a crucial step in identifying and fabricating materials with lower noise levels. $1/f$ noise has been observed in many systems, including metals, semiconductors, and various devices. The underlying physical mechanism of the observed ubiquitous $1/f$ noise remains subject to intense debate. However, a system exhibiting $1/f$ noise must have a broad distribution of time scales in its nonequilibrium dynamics. Because electron energy varies greatly from site to site in these systems, electron hopping between neighboring sites is a highly stochastic process, which involves diverse time scales. We found that these diverse time scales in the hopping conduction can give rise to $1/f$ noise over an extended frequency range, which is further widened if the system exhibits a strong Meyer-Neldel behavior.

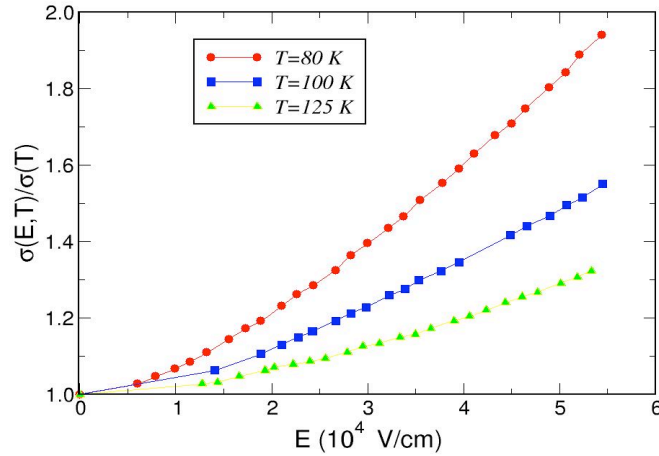


Figure 18. Normalized conductivity, $\sigma(E,T)/\sigma(T)$, as a function of applied electric field E for different temperatures measured in $\text{VO}_{1.8}$. Data were measured by Dr. Roger

7.1 MODEL AND APPROACH

The excellent agreement between theory and experiment on electrical transport suggested that this lattice model captures essential physics of VO_x and was a good starting point to study $1/f$ noise. To model $1/f$ noise, we examined the time evolution of the system under a random external input. Specifically, the time-dependent carrier occupation at site i , $f_i(t)$, is described by the differential equation,

$$\frac{df_i}{dt} = \sum_j [f_j(1 - f_i)w_{ji} - f_i(1 - f_j)w_{ij}] - g_i(t), \quad (7.1)$$

where $g_i(t)$ is a random function and w_{ij} is the hopping probability from site i to site j , which can be expressed as

$$w_{ij} = \nu \exp(-2\alpha R) e^{(\varepsilon_i - \varepsilon_j)/2k_B T}, \quad (7.2)$$

where k_B is the Boltzmann constant and T the temperature, ε_i is the carrier energy at site i , $R = |\mathbf{r}_i - \mathbf{r}_j|$ is the distance between sites i and j , α^{-1} is the localization length of electrons, and ν is the frequency of electron hopping attempts.

A change in the carrier occupation f_i can be described equivalently by a deviation of the chemical potential μ_i from its equilibrium value (Fermi level) μ_0 , and in the linear-response regime,

$$\delta f_i(t) = \beta(\mu_i - \mu_0) f_i^0 (1 - f_i^0) \equiv \beta \xi_i f_i^0 (1 - f_i^0), \quad (7.3)$$

where $\beta = 1/k_B T$. The above differential equations become linear

$$f_i^0 (1 - f_i^0) \frac{d\xi_i}{dt} = \sum_j \left[w_{ji} f_j^0 (1 - f_i^0) \xi_i - w_{ij} f_i^0 (1 - f_j^0) \xi_j \right] - f_i^0 (1 - f_i^0) \eta_i(t), \quad (7.4)$$

where $g_i(t) \equiv f_i^0 (1 - f_i^0) \eta_i(t)$. The above equations can be written as

$$\frac{d\xi_i}{dt} - \sum_j A_{ij} \xi_j = \eta_i(t), \quad (7.5)$$

where the matrix A_{ij} is

$$A_{ij} = \frac{1}{f_i^0 (1 - f_i^0)} \left(\left[\sum_k w_{ki} f_k^0 (1 - f_i^0) \right] \delta_{ij} - w_{ij} f_i^0 (1 - f_j^0) \right). \quad (7.6)$$

The time evolution of ξ_i is largely determined by the eigen modes of matrix \mathbf{A} . For the k th mode, the eigenvalue λ_k and its corresponding eigenvector \mathbf{x}_k satisfy

$$\mathbf{A} \mathbf{x}_k = \lambda_k \mathbf{x}_k. \quad (7.7)$$

And the chemical-potential fluctuation in the system, written as $\boldsymbol{\xi} = (\xi_1, \dots, \xi_N, \dots)^T$, is a linear combination of the eigen modes,

$$\boldsymbol{\xi} = \sum_k \xi_k \mathbf{x}_k. \quad (7.8)$$

Hence we can write the above differential equations in terms of the independent modes

$$\frac{d\xi_k}{dt} - \lambda_k \xi_k = \eta_k(t), \quad (7.9)$$

and its Fourier transform in the frequency space

$$i\omega\tilde{\xi}_k(\omega) - \lambda_k\tilde{\xi}_k(\omega) = \tilde{\eta}_k(\omega). \quad (7.10)$$

If we consider each input pulse η_k as an independent random event,

$$\langle \eta_k(t)\eta_k(t') \rangle = D_k\delta(t-t') \quad (7.11)$$

where D_k is the averaged intensity of the random pulses for the k th mode. The spectral density of η_k is $w_k(f \equiv \omega/2\pi > 0)$, according to the Wiener-Khintchine theorem,

$$w_k(f) = 2\overline{\tilde{\xi}_k(\omega)\tilde{\xi}_k(-\omega)} = \frac{2D_k}{\omega^2 + \lambda_k^2}. \quad (7.12)$$

To determine D_k , we use the equipartition law, that the chemical-potential (voltage) fluctuation in a circuit is

$$\frac{1}{2}C\overline{\xi_k^2} = \frac{1}{2}k_B T = \int_0^\infty df w_k(f) = \frac{D_k}{2\lambda_k}, \quad (7.13)$$

where C is the capacity of the circuit. We have $D_k = 2k_B T \lambda_k / C$. The total spectral density, including all the modes, is then

$$w(f) = \sum_k w_k(f) = \sum_k \frac{4k_B T}{C} \frac{\lambda_k}{\omega^2 + \lambda_k^2}. \quad (7.14)$$

Thus, to calculate the noise spectrum, we need to find all the eigenvalues of the matrix A . It is easy to see that one eigenvalue is $\lambda_0 = 0$, which corresponds to the equilibrium situation, where f_i follows the Fermi-Dirac distribution with the Fermi level at μ_0 . All other eigenvalues must be negative, $\lambda_k < 0$, because any fluctuation will decay over time.

7.2 MEYER-NELDEL RELATION

In VO_x and many other disordered materials, the Meyer-Neldel relation has been observed. If the temperature-dependent conductivity is written as

$$\sigma(T) = \sigma_0 e^{-E_a/k_B T}, \quad (7.15)$$

the prefactor σ_0 is found to exponentially increase with the activation energy E_a ,

$$\sigma_0 \propto e^{E_a/k_B T_{MN}} \quad (7.16)$$

where T_{MN} is the Meyer-Neldel temperature. In VO_x , from fitting to the conductivity data for a variety of VO_x ranging from $x = 0.8$ to $x = 1.8$, $T_{MN} = 801$ K is obtained.

To date, no theory satisfactorily explains the seemingly universal Meyer-Neldel relation. One plausible argument is that as the energy barrier E_a for electron hopping increases, the possible

paths for the hopping quickly grow. The observed Meyer-Neldel relation in VO_x suggests that the prefactor ν in Eq. (7.2) should not be a constant, but, rather, a function of the energy difference between the two sites,

$$w_{ij} = \nu_0 e^{(\varepsilon_i - \varepsilon_j)/k_B T_{MN}} \exp(-2\alpha R) e^{(\varepsilon_i - \varepsilon_j)/2k_B T} \quad (7.17)$$

We consider a cubic lattice with $32 \times 16 \times 16$ sites and the lattice constant $a = 3 \text{ \AA}$. First we generate the site energy ε_i , a random that follows a certain distribution and then calculate the matrix \mathbf{A} . Then we find all the eigenvalues λ_k of \mathbf{A} and compute the spectral density $w(f)$ according to Eq. (7.14). The matrix \mathbf{A} is large, with dimension of 8192^2 , and has 8191 negative λ_k . All the calculations presented in this paper are for room temperature, $T = 300 \text{ K}$.

Figure 19 shows the calculated noise spectral density $w(f)$ as a function of dimensionless ω/ν_0 for different Meyer-Neldel temperatures. We see that the spectral density is virtually a constant at very low frequencies and has an asymptotic behavior of $1/\omega^2$ at very high frequencies. There is an intermediate range that the spectral density has an approximately $1/\omega$ dependence. From Fig. 19, the frequency range where the noise shows a $1/f$ behavior strongly depends on the Meyer-Neldel temperature, T_{MN} . For a system with a strong Meyer-Neldel behavior, i.e., small T_{MN} , the $1/f$ noise persists over a broad frequency range.

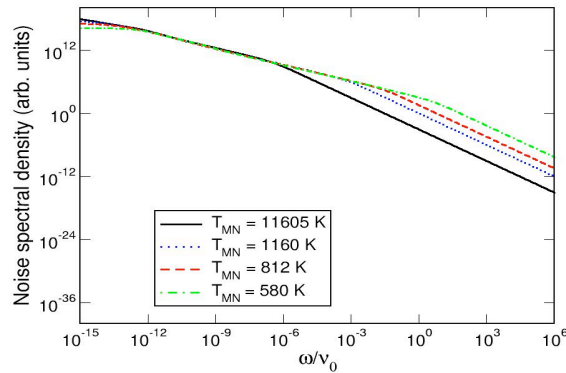


Figure 19. Noise spectral density $w(f)$ as a function of ω/ν_0 for different Meyer-Neldel temperatures. The site energy is uniformly distributed in $[-\Delta, \Delta]$ with $\Delta = 0.5 \text{ eV}$, and the Fermi energy is -0.3 eV . The electron localization parameter is set $\alpha = 5 \text{ \AA}^{-1}$.

If we assume that the noise spectral density has a power-law dependence on the frequency,

$$w(f) = w_0 \omega^\gamma, \quad (7.18)$$

the exponent γ can be obtained from

$$\gamma = \frac{d \ln w}{d \ln \omega}. \quad (7.19)$$

Figure 20 plots the exponent γ as a function of ω/ν_0 from the spectral densities illustrated in Fig. 19 and clearly shows the frequency range of $1/f$ noise where $\gamma \approx -1$.

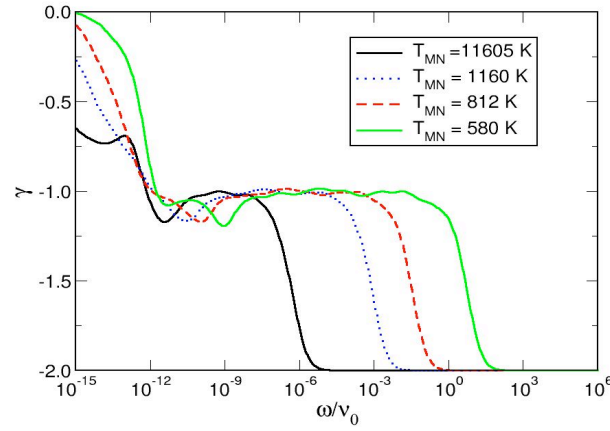


Figure 20 Exponent γ as a function of ω/ν_0 obtained from Fig. 19.

Because the noise spectral density is determined by the eigenvalues λ_k of matrix A , according to Eq. (7.14), different noise behaviors indicate different distributions of these eigenvalues. Figure 21 plots the distribution of $\ln |\lambda_k|$ for these different Meyer-Neldel temperatures. For a system showing a strong Meyer-Neldel behavior, the eigenvalues λ_k and their associated time scales $-1/\lambda_k$ have a broad distribution.

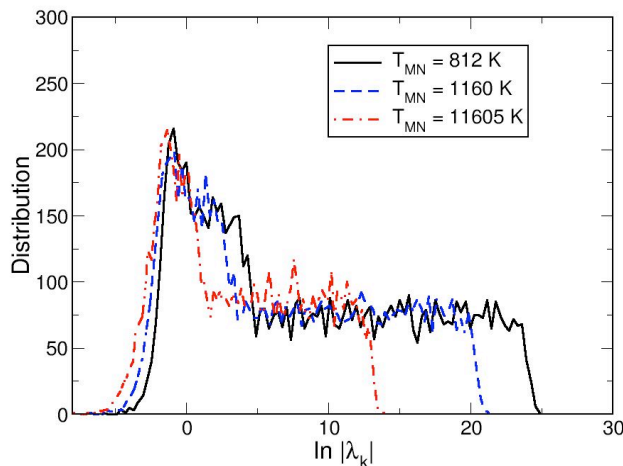


Figure 21 Distribution of $\ln|\lambda_k|$ for different Meyer-Neldel temperatures. The parameters are as shown in Fig. 19.

8. COHERENCE DYNAMICS OF PHOTOSYNTHESIS

Recent multicolor photon-echo experiments revealed a long-lasting quantum coherence between excitations on donors and acceptors in photosynthetic systems. Identifying the origin of the quantum coherence is essential for fully understanding photosynthesis. In our generic model, a strong intermolecular steric restoring force in densely packed pigment-protein complexes results in a spatial correlation in conformational (static) variations of chromophores, which in turn induces an effective coupling between high-frequency (dynamic) fluctuations in donor and acceptor. The spatially correlated static and dynamic fluctuations provide a favorable environment for maintaining quantum coherence, which consistently explains the photon-echo measurements. Of note, the macroscopic and primitive elastic energy, when acting collectively, can provide a favorable environment for protecting the microscopic and delicate quantum coherence in strongly fluctuating biological systems. Figs. 22 and 23 compare our calculated photon-echo signals with experimental results.

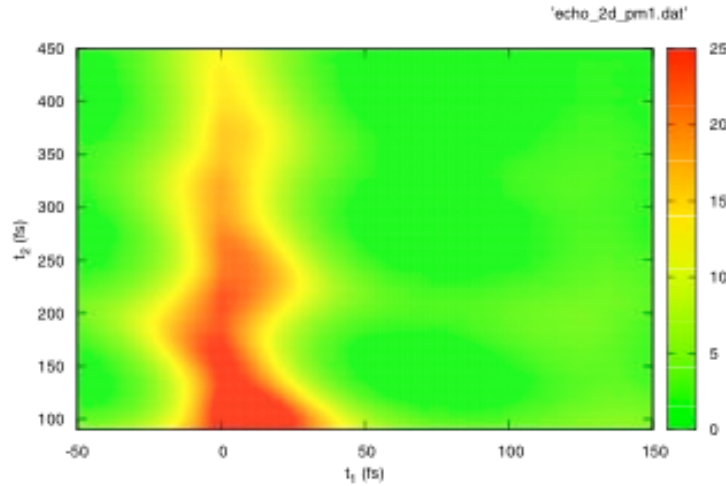


Figure 22. Photon-echo signals obtained from our calculations.

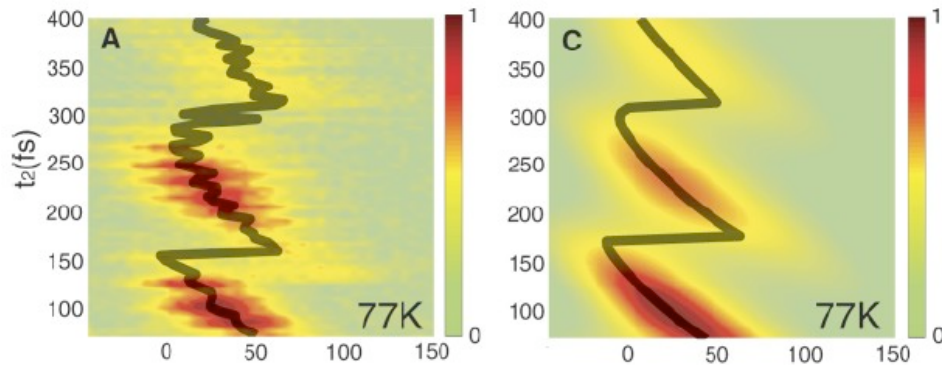


Figure 23. Photon-echo signals obtained from experiments.

COLLABORATION WITH ACADEMIA AND INDUSTRY

Because of the importance of uncooled IR detection to the military, the Department of Defense has made significant investments in perfecting microbolometer technology and is funding projects at several companies and universities to study VO_x. To share our results and insights gained from this project, we worked closely with both experimentalists and theorists in the MURI team to analyze experimental data and model VO_x systems from first-principles calculations. In particular, we analyzed the AC conductivity data from Prof. Mark Horn's group, and provided strategies for modeling VO_x defect structures through first-principles calculations. We suggested pertinent experiments to understand transport in VO_x and α -Si thin films based on our modeling results, and gained insight into these systems. Prof. Mark Horn from Penn State University, Dr. A. J. Syllaios, and Dr. Mingliang Zhang, a postdoc from Prof. David Drabold's group at Ohio University visited SRI during the last two years.

PUBLICATIONS

Z. G. Yu, M. A. Berding, and H. Wang, “Spatially correlated fluctuations and coherence dynamics in photosynthesis,” *Phys. Rev. E* 78, 050902 (Rapid Communications) (2008).

M. A. Berding and Z. G. Yu, “Defect microstructures and their effects on electrical transport in VO_x,” *Proc. MSS 2006*.

M. A. Berding, Z. G. Yu, and R. E. DeWames, “Electronic structures, optical absorption, and electrical transport in VO_x,” *Proc. MSS 2007*.

Z. G. Yu and M. A. Berding, “Carrier transport under strong electric fields in VO_x for microbolometers,” *Proc. MSS 2009*.

R. DeWames, Z. G. Yu, and D. Lohrman, “Electrical conduction and long relaxation times in non-crystalline VO_x and α-Si:H microbolometer infrared detectors,” *Proc. MSS 2010*.

Z. G. Yu and M. A. Berding, “Numerical simulation of $1/f$ noise in VO_x for microbolometers,” *Proc. MSS 2010*.

R. E. DeWames, A. J. Syllaos, Z. G. Yu, and M. A. Berding, “Distinct electrical transport mechanisms in noncrystalline VO_x and a-Si:H,” to be submitted to *Appl. Phys. Lett.*

CONFERENCE PRESENTATIONS

Z. G. Yu, “Spatially correlated fluctuations and coherence dynamics in photosynthesis,” 2009 APS March Meeting, Pittsburgh, Pennsylvania, March 16-20, 2009.

RECOGNITION OF RESEARCH ACCOMPLISHMENTS

Our paper, “Carrier transport under strong electric fields in VO_x for microbolometers,” was selected as the best paper at the 2009 MSS workshop.